

Article

# A Long-Term Passive Microwave Snowoff Record for the Alaska Region 1988–2016

Caleb G. Pan <sup>1,2,\*</sup> , Peter B. Kirchner <sup>2,3</sup> , John S. Kimball <sup>2</sup> and Jinyang Du <sup>2</sup><sup>1</sup> RedCastle Resources, Inc., Salt Lake City, UT 84138, USA<sup>2</sup> Numerical Terradynamic Simulation Group, University of Montana, Missoula, MT 59801, USA; peter\_kirchner@nps.gov (P.B.K.); johnk@ntsg.umt.edu (J.S.K.); jinyang.du@mso.umt.edu (J.D.)<sup>3</sup> Southwest Alaska Network Inventory and Monitoring Program, National Park Service, Anchorage, AK 99501, USA

\* Correspondence: caleb.pan@mso.umt.edu

Received: 3 November 2019; Accepted: 24 December 2019; Published: 2 January 2020



**Abstract:** Snowoff (SO) date—defined as the last day of observed seasonal snow cover—is an important governor of ecologic and hydrologic processes across Alaska and Arctic-Boreal landscapes; however, our understanding and capacity for the monitoring of spatial and temporal variability in the SO date is still lacking. In this study, we present a 6.25 km spatially gridded passive microwave (PMW) SO data record, complimenting current Alaskan SO records from Moderate Resolution Imaging Spectrometer (MODIS) and Landsat, but extending the SO record an additional 13 years. The PMW SO record was validated against in situ snow depth observations and showed favorable accuracy (0.66–0.92 mean correlations; 2–10 day mean absolute errors) for the major climate regions of Alaska. The PMW SO results were also within 10 days of finer spatial scale SO observational records, including Interactive Multisensor Snow and Ice Mapping System (IMS), MODIS, and Landsat, for a majority (75%) of Alaska. However, the PMW record showed a general SO delay at higher elevations and across the Alaska North Slope, and earlier SO in the Alaska interior and southwest regions relative to the other SO records. Overall, we assign an uncertainty  $\pm 11$  days to the PMW SO. The PMW SO record benefits from the near-daily temporal fidelity of underlying brightness temperature (T<sub>b</sub>) observations and reveals a mean regional trend in earlier SO timing ( $-0.39$  days yr<sup>-1</sup>), while significant ( $p < 0.1$ ) SO trend areas encompassed 11% of the Alaska domain and ranged from  $-0.11$  days yr<sup>-1</sup> to  $-1.31$  days yr<sup>-1</sup> over the 29-year satellite record. The observed SO dates also showed anomalous early SO dates during markedly warm years. Our results clarify the pattern and rate of SO changes across Alaska, which are interactive with global warming and contributing to widespread permafrost degradation, changes in regional hydrology, ecosystems, and associated services. Our results also provide a robust means for SO monitoring from satellite PMW observations with similar precision as more traditional and finer scale observations.

**Keywords:** snow cover; snowoff; snow melt; passive microwave; Alaska; Arctic

## 1. Introduction

Snow is a defining regulator of the global energy budget and ecosystem function, governing both ecologic and hydrologic responses to climate variability. Warming across the high latitudes in the Northern Hemisphere has contributed to reduced snow cover [1], whereby the reduced surface albedo from less snow cover [2,3] enhances the solar energy loading that promotes additional thawing that reinforces further climate warming [1,4–6]. In Alaska, the snow-free season has lengthened, prompting a cascade of environmental impacts [3], including earlier onset of snowmelt and seasonal flooding in spring; earlier and longer potential growing seasons [7,8]; changes in

permafrost active layer conditions, vegetation growth, and ecosystem net carbon uptake [9,10]; and reductions in plant diversity [11,12]. Quantifying the spatial and temporal trends in regional snow cover changes is important for better understanding the regional impacts of a warming climate on boreal-Arctic ecosystems.

Snow cover assessments can be obtained from models, in situ observations, remote sensing, or a combination of these. In Alaska, snow has been modeled using climate data products including the Parameter Elevation Relationships on Independent Slope Model (PRISM) and the Modern-Era Retrospective analysis for Research and Applications (MERRA-2) [13,14]. These products are often limited by coarse spatial resolution (1–50 km) and/or limited spatial coverage. The Alaska Snow Telemetry (SNOTEL) network provides high quality in situ snow measurements of depth, density, and snow water equivalent (SWE); however, the utility of these measurements is limited by a very sparse station distribution in northern, boreal-arctic ecosystems that is inadequate to represent landscape heterogeneity and snow redistribution mechanisms [1,15–17]. Remote sensing offers a remedy to the limitations of both modelled and in situ snow observations for regional assessment and monitoring of snow conditions. A variety of satellite platforms and sensor types have been used for the remote sensing of snow, including passive optical-infrared sensors [30–500 m], Lidar [~1 m], microwave Radars and scatterometers [25 km], and passive microwave radiometers [25 km]. Each sensor type is sensitive to different snow properties, while providing variable sampling footprints, accuracy, and spatial and temporal coverage.

Snow properties derived from remote sensing observations include: snow covered area [18–20], snow depth [21,22], SWE [23], main melt onset [24,25], and snow wetness [26]. Determining the date of snowoff (SO)—defined here as the last day of observed seasonal snow cover in spring—is particularly valuable from an ecosystem perspective because it is tractable and is a key metric influencing other environmental variables, including: the start of spring carbon uptake, snowmelt duration [8,27], wildlife ecology and movement [17], and the timing of hydrologic events [28]. SO has been defined using several terms, including but not limited to: snow disappearance [29], snow clearance day [9], melt-off day [30], and snow persistence [31]. Optical remote sensing methods have generally determined SO using a threshold value of single channel spectral reflectance data or channel combinations such as the Normalized Difference Snow Index (NDSI) [32].

Relatively high-quality SO data products with spatial projections for Alaska include the Alaskan MODIS Snow Cover Metrics and Landsat Snow Persistence Maps. The Alaskan Snow Cover Metrics are a suite of complimentary snow parameters derived from the Moderate Resolution Imaging Spectrometer (MODIS) at 500 m spatial resolution, with SO defined as the last day of the longest continuous snow season (LCLD) [13]. The annual Alaskan Landsat Snow Persistence Maps represent the last day snow persisted, and have a native 30 m spatial resolution and observational record that extends from 2001 to present [31]. Despite the good overall quality of these products, there is inherent uncertainty introduced from infrequent image acquisition intervals (i.e., 16-day for Landsat) and coarse temporal compositing of the optical-infrared sensor retrievals required to mitigate contaminating effects from clouds and atmosphere aerosols, low solar illumination at higher latitudes ( $\geq 45^\circ\text{N}$ ), and the inherent errors associated with optical remote sensing of snow [33]. Furthermore, both the MODIS and available Landsat snow products have a temporal record beginning in 2001, making it difficult to evaluate longer-term trends and variability.

Satellite passive microwave (PMW) sensors offer several advantages over optical sensors because they provide global daily coverage and are insensitive to potential signal degradation from low solar illumination and atmosphere cloud-aerosol contamination [34]. Furthermore, PMW sensors, including the Defense Meteorological Satellite Program (DMSP) Special Sensor Microwave Imager (SSM/I) (1987–present) and Special Sensor Microwave Imager/Sounder (SSMIS) (2004–present), are sensitive to snow cover properties and provide continuous global observations from similar overlapping satellites extending as far back as 1987. SO has been calculated from PMW retrievals using several approaches, including snow cover duration (SCD) [9], spring thaw timing [35,36],

wavelet transformations of brightness temperature (Tb) time series [27], Tb diurnal amplitude variations (DAV) [37,38], and Tb differencing algorithms [30,39]. A common physical basis for snow retrieval among these methods is the differential response in microwave emissions at 19 (V, H) GHz and 37 (V, H) GHz frequencies to changes in liquid water content of the surface snowpack.

Optical and PMW sensors both have limitations for effective snow retrievals. Variable snow cover reflectance properties in complex terrain, overlying vegetation cover, unfavorable lighting, and persistent cloud-atmosphere aerosol contamination can severely constrain optical remote sensing of snow cover in the boreal-Arctic. While many of these limitations are reduced or minimized from PMW remote sensing, the microwave snow retrievals are affected by other constraints including a relatively coarse sampling footprint required to achieve an adequate signal-to-noise ratio, and the contaminating influence of open water, underlying soil, and dense vegetation within the sensor footprint. The resulting satellite snow products can show inconsistent results even for the same snow metrics because of the differences in the underlying sensor characteristics and retrieval algorithms [13]. In this study, we developed a new satellite SO record for Alaska using PMW daily 19V (K-band) and 37V (Ka-band) GHz Tb observations extending from 1988–2016. We used a spatially enhanced Special Sensor Microwave Imager Sounder (SSM/I(S)) Tb record for the SO retrievals, with four-fold (6.25 km resolution) improved spatial gridding for delineating regional snow patterns relative to the SSM/I(S) native footprint retrievals [25 km]. The PMW SO record is validated against in situ snow depth observations from regional weather stations and compared with other available regional SO records derived from MODIS, Landsat, and model-based assessments. The objectives of this study are to: (i) elucidate the roles of fractional water inundation, forest cover, and topographic complexity as sources of uncertainty as compared to in situ observations and other remote sensing SO products; and (ii) investigate recent SO regional trends enabled from a longer (29-year) satellite PMW record. A major premise for this study is that the satellite PMW record provides daily temporal fidelity and moderate spatial resolution, enabling better SO accuracy and performance relative to other available SO records from satellite optical remote sensing.

## 2. Study Area and Materials

Alaska spans a large area, approximately 20° of latitude and 50° of longitude, encompassing the North Pacific, Arctic Boreal, and Arctic Ocean regions of the extratropical (>50°N) Northern Hemisphere. Within this region, multiple gradients influence the climate, including latitude, distance from large water bodies, the relative thermal mass and circulation of coastal waters, the location and orientation of major mountain ranges, and elevation. With over 10,000 km of coastline, the region is bounded by the Pacific Ocean to the south and the shallower, seasonally ice-covered Bering, Chukchi and Beaufort seas to the west and north that provide sources of moisture and thermal gradients that drive seasonal weather. This high latitude region also plays an important role in the earth's energy, water and carbon cycles, and is highly vulnerable to recent climate warming [3,40]. Much of the region is snow covered for 6 to 9 months of each year; thus snow is an integral component of the ecosystem and a phase change from snow to rain has potentially profound implications for ecosystem structure and function. Thirteen climate divisions have been described for the state of Alaska [41], which we aggregated into three broader regions for the spatial SO analysis, including Interior, Western and North Slope domains (Figure 1). These domains reflect Alaska's major climatic regimes representing moderate Pacific maritime, cold-dry boreal interior, and polar arctic northwest coast and North Slope climate zones. The spatial extent of the PMW-derived SO record from this study includes Alaska, the Russian Far East, and northwest Canada (See Supplementary materials); however, our comparative analysis covers a smaller domain defined by the Landsat snow persistence product [31].

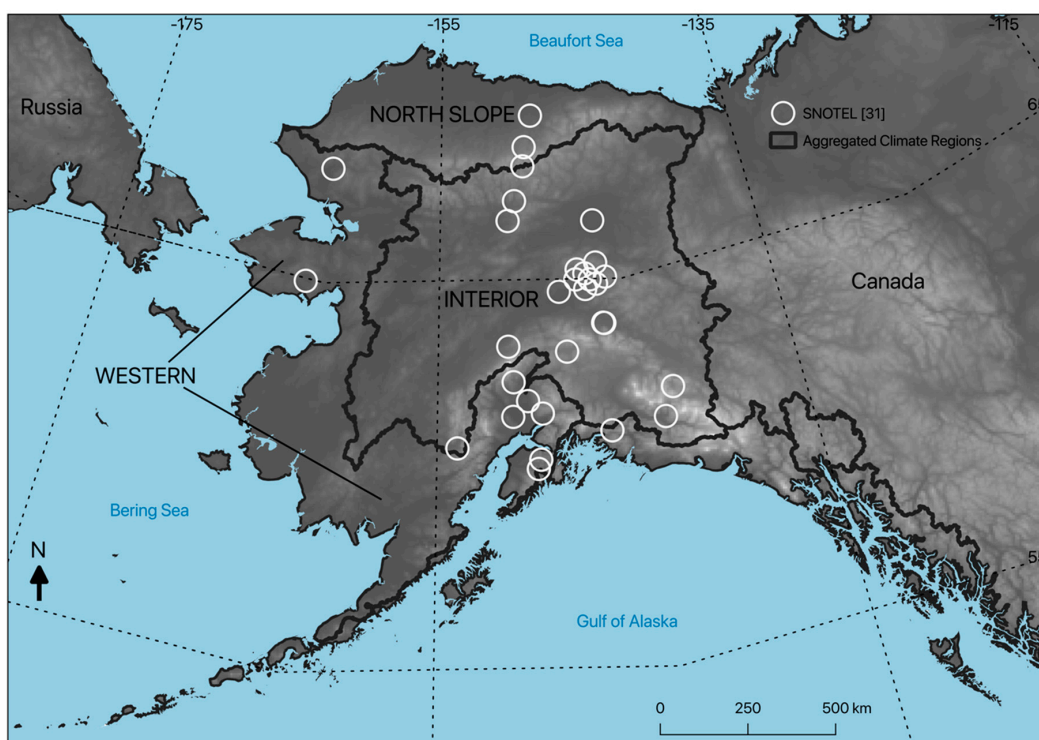


**Figure 1.** Spatial extent of the new passive microwave snowoff (SO) data product, aggregated climate regions used in the analysis (western, North Slope, and the Interior) and the locations of in situ Snow Telemetry (SNOTEL) station observations.

### 2.1. Passive Microwave Record 1988–2016

We detected SO using the SSM/I(S) 19 and 37 GHz ascending orbit (~17:00 local solar time) Tb retrievals at horizontal (H) and vertical (V) polarizations from the MEASUREs Calibrated Enhanced-Resolution Passive Microwave Daily EASE-Grid 2.0 Brightness Temperature ESDR, available at the National Snow and Ice Data Center (NSIDC) [42]. This data record is a temporally extensive consortium of images from multiple sensors and platforms. The spatial resolution of the 19 and 37 GHz Tb channels used in this study are improved from the original 25-km resolution Tb format through spatially enhanced interpolation of overlapping Tb antenna patterns and regridding at 6.25 km (19 GHz) and 3.125 km (37 GHz) resolution in a northern polar EASE-grid format using the scatterometer image reconstruction (SIR) technique [43].

The SSM/I(S) Tb retrievals from different DMSP satellite platforms are highly correlated and only small improvements are made using correction techniques [44], allowing us to use overlapping observations from the DMSP F-series satellites during the SSM/I and SSMIS era to gap-fill missing coincident grid cells using a nearest-neighbor substitution. Any remaining missing days were gap-filled using a temporal linear interpolation [25]. The gap-filled daily Tb retrievals were clipped and reprojected to the Alaska Albers Conical Equal Area Projection using the North American Datum 1983 to match the same spatial extent and projection as the MODIS derived snow metrics for Alaska [13].

### 2.2. Deriving SO

We use the 19V–37V Tb differencing as the primary approach to detect SO [45], defined here as the last day of snow cover in spring. The resulting Tb difference is strongly positive and relatively stable prior to the seasonal onset of snowmelt indicated from in situ weather station observations (Figure 2). However, once the snow begins to melt the Tb difference between the two channels precipitously decreases, mirroring the snow ablation rate before reaching a seasonal minimum and becoming more temporally stable following snowoff and moving into the summer. The Tb difference

reaches a seasonal minimum just after the snow has finished ablating, which we use to represent the SO condition. We observe a larger positive Tb difference between 19V and 37V GHz channels under colder winter temperatures because the emissivity is greatest at 19V relative to 37V in dry snow conditions. The Tb frequency difference is minimized as snow depth decreases and the liquid water content of the snowpack increases. Shortly after snowpack depletion the land surface is relatively wet and the microwave emissivity is generally larger at 37V than 19V GHz [46,47]; hence we define SO as the date when the 19V and 37V difference is at its lowest.

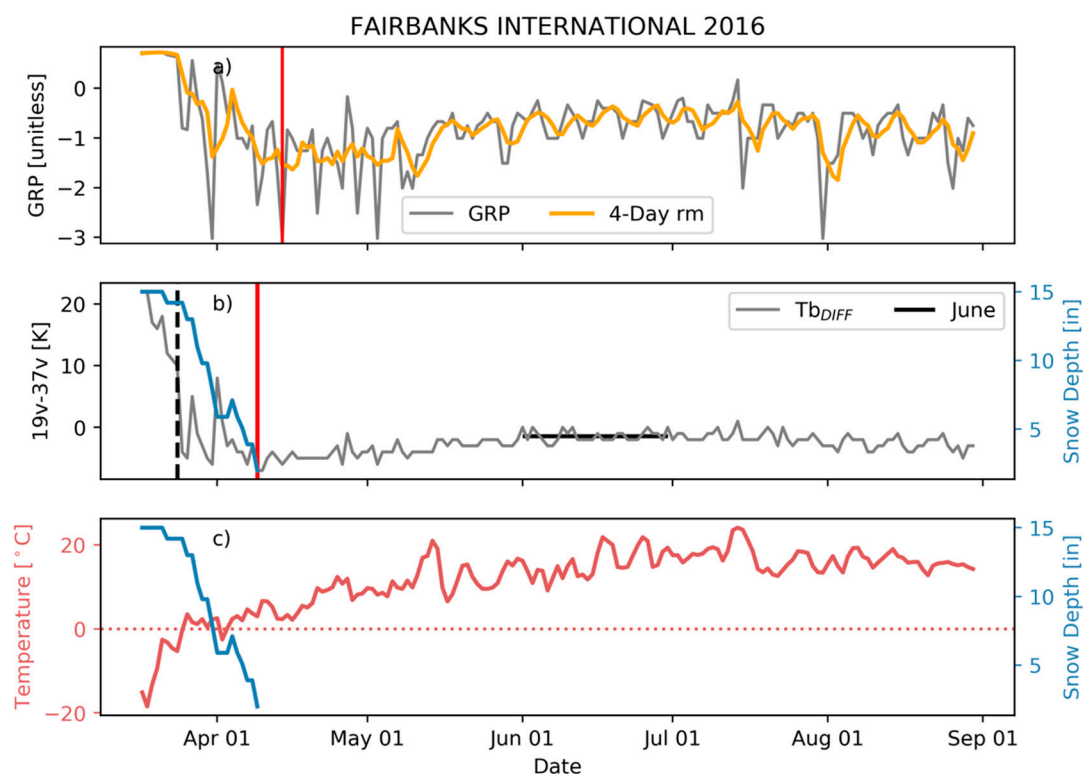


**Figure 2.** Example Special Sensor Microwave Imager (SSM/I) gradient ratio polarization (GRP) time-series over Fairbanks International Airport ( $64^{\circ}48'59''\text{N}$ ,  $147^{\circ}51'49''\text{W}$ ) for the 2016 water year: (a) daily GRP (grey) and 4-day running mean (orange); (b) Tb difference (grey) with average Tb difference during June denoted by the horizontal black line. In both (a) and (b), the black vertical dashed line shows beginning of melt and the vertical red bars represent the calculated SO date for each method. (c) Daily average air temperature (red) and snow depth (blue).

We use a dynamic Tb differencing approach by first calculating the average annual Tb difference value (*sum*) for June, which is used as a threshold to identify possible SO dates. We then classify the SO date where the daily Tb difference is less than *sum* and has the lowest value of all other potential selections (Figure 2). We found that the Tb differencing approach was unable to provide reliable SO detection in coastal grid cells, which was attributed to greater water body contamination of the Tb retrievals over adjacent land areas [48]. The affected grid cells represent 2–3% of the study domain per year. For these instances we used an alternative gradient ratio polarization (GRP) algorithm [26,49] to detect SO. For the GRP approach, SO was classified for each grid cell as the day with lowest 4-day running GRP mean (rm) over each seasonal cycle (January–July).

### 2.3. Gridded SO Datasets

In addition to validating the PMW SO dates against SNOTEL measurements, we also compare the PMW SO with other satellite-derived Alaskan SO dates. The comparisons are quantified as residuals

(days) showing the location and magnitude of PMW SO occurring earlier or later relative to the other SO records.

### 2.3.1. Alaskan Snow Metrics from MODIS

The Alaskan Snow Metrics cover Alaska, northwestern Canada, and the Russian Far East. The data originate from the MODIS Terra Snow Cover Daily L3 Global 500 m Grid data (MOD10A1) [50] from 2001–2016. The data are provided annually as 12 band GeoTIFFs—each band representing a different snow cover metric. The MODIS MOD10A1 product is a binary snow cover extent dataset derived from the NDSI. Data processing involves a 3-step filtering process to fill the data gaps, including a spatial and temporal filter, as well as a snow cycle filter [13]. In this study, we used the last day of continuous snow cover (LCLD) to represent SO and resampled each GeoTIFF image using the median LCLD value to match the same 6.25 km resolution and dimensions as the PMW-derived SO record.

### 2.3.2. Alaskan Snow Persistence

Snow persistence is defined as the transition from snow to snow-free surface conditions. The Alaskan annual snow persistence maps begin in 2001 and are roughly constrained to the Alaskan state boundaries [31]. This dataset is derived from Landsat (TM, ETM+, OLI) observations and provides a relatively high-resolution (30 m) estimation of annual SO across Alaska. After shadows and clouds are filtered from the 16-day Landsat optical reflectance data, daily snow cover extent is calculated using the NDSI. The remaining unmasked NDSI time series is then used in a regression tree model to predict SO in days of year (DOY) for each 30m grid cell [31]. The Landsat 30 m Alaska SO record used in this study extended from 2001–2017 and was resampled using the median value and returned the same 6.25 km grid projection as the PMW SO record. We also assigned a minimum +/-16 day precision threshold to the Landsat SO record based on the Landsat 16-day potential sampling frequency, which was used to assess the relative performance of the PMW SO record developed from this study.

### 2.3.3. IMS

The Interactive Multisensor Snow and Ice Mapping System (IMS) daily snow cover extent record covers different years and spatial grid formats, including 1 km (2014–present), 4 km (2004–present), and 24 km (1997–present) resolutions across the Northern Hemisphere. The IMS snow data are derived using expert interpretation of geostationary visible satellite imagery, polar orbiting multispectral satellite sensors, PMW sensors, and ground observations [51,52]. The IMS daily snow cover extent is one of the highest performing snow cover products available, likely attributed to its use of a trained analyst in combination with automated classifications and inclusion of ground observations, which decrease the influence of clouds [53]. In this study, we used the 4 km IMS snow cover extent product and calculated SO as the first day of 14 consecutive days of snow free conditions for each grid cell [30]. We assigned a +/-14 day precision threshold to the IMS derived SO record based on the 14-day moving window classification, which was used as a basis for evaluating our PMW SO record. The IMS data were also resampled to the same PMW 6.25 km resolution format using the median value. A summary of each satellite SO dataset used in this study is given in Table 1.

**Table 1.** Alaska regional snow cover products used for the SO evaluation in this study.

Dataset	Native Spatial Resolution	Period of Record	Coverage	Source Data Types	Resource
IMS	4 km	2004–2017	Northern Hemisphere	PMW, Optical, in Situ Observations	Helfrich et al. 2007
Landsat Snow Persistence	30 m	2001–2017	Alaska (southeast excluded)	Landsat	Macander and Swingley 2017
MODIS Snow Metrics	500 m	2001–2016	Russia Far East, Alaska, Northwest Canada	MODIS	Lindsay et al. 2015
PMW	6.25 km	1988–2016	Russia Far East, Alaska, Northwest Canada	PMW	This Study

#### 2.4. Ancillary Datasets

In situ snow depth observations were used to validate the PMW SO algorithm and compare uncertainty between each SO dataset. Like the IMS SO, we defined in situ SO as the first day of 14 consecutive days where snow depth was zero. We used snow depth observations from 31 SNOTEL stations across Alaska and constrained our validation and comparison period to 2004–2016, the common period that all gridded SO datasets share.

We examined the influence of three land surface properties potentially influencing the PMW SO accuracy, including surface fractional water inundation (FW), fractional forest cover (FF), and the elevation gradient within a grid cell [54,55]. We used the dynamic 5-km FW record derived from the Advanced Microwave Scanning Radiometer sensors (AMSR-E and AMSR2), calculated as 10-day FW outputs [56]; the FW record used here is derived from higher frequency (89 GHz) Tb retrievals than the PMW SO record, but has similar spatial resolution and microwave sensitivity to surface water. We calculated the annual mean FW cover during the summer months from 2002 to 2015 for each grid cell. The PMW performance was then evaluated along a regional gradient in surface water conditions based on the FW summer mean and coefficient of variation (CV) (Figure 3). Grid cells with significant open water cover ( $FW > 5\%$ ) were masked from the SO validation to reduce the effect of surface water contamination of the Tb retrievals [57]. We also excluded grid cells where the FW exceeded a 70% CV threshold, indicating areas with large summer inundation variability. The total area excluded by the FW screening represented approximately 14% of the study domain (Figure 3c). We also masked out perennial snow/ice areas identified in the Landsat snow persistence images, which represented an additional of the Alaska domain.

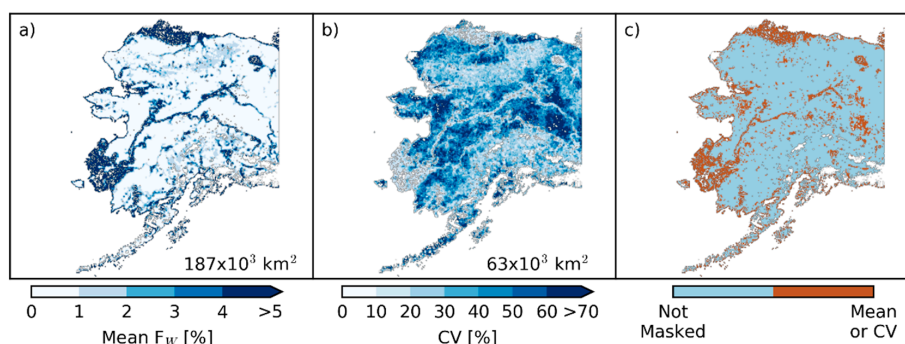


**Figure 3.** 2002–2015 mean fractional water (FW) (a), FW coefficient of variation (CV) (b) note high variability in central North Slope and Interior and FW mask (c) where brown indicates masked area that meets either the mean or CV condition.

The MODIS MOD44B V005 Vegetation Continuous Fields (VCF) product was used to represent the percent tree cover (FF) within each 6.25 km SO grid cell, as defined from the MODIS 250 m native VCF pixel resolution. The VCF has an estimated error of  $\pm 11.5\%$  and is acceptable for our applications [58]. We also used the GTOPO30 digital elevation model (DEM) with 1 km native resolution to calculate the topographic complexity (TC) within each 6.25 km SO grid cell; where TC was calculated as the spatial standard deviation of the elevation within a cell.

## 2.5. Assessing the Performance of the PMW SO Algorithm

### 2.5.1. SNOTEL Validation

The PMW SO results were validated against SO estimates derived from in situ daily weather station observations from Alaska NRCS SNOTEL sites (Table A1). The mean absolute error (MAE) was derived between each SNOTEL site based SO estimate and the satellite SO retrieval from the overlying PMW grid cell for each site location. Similar MAE metrics were also calculated for the MODIS, Landsat, and IMS SO datasets at each SNOTEL location. The MAE results were then used to evaluate PMW SO accuracy and performance relative to the other SO geospatial products. We also aggregated the SNOTEL annual SO results within each climate region. The SO correlation, MAE and root mean square error (RMSE) differences were then calculated for each climate region between the aggregated SNOTEL observations (independent variable) and the corresponding PMW results (dependent). The same statistics were calculated for the MODIS, Landsat, and IMS-based SO results, and used to evaluate PMW performance relative to the other datasets.

### 2.5.2. Residuals and Uncertainty

Pixel-wise residuals were calculated to quantify the sign and magnitude of differences between the PMW SO algorithm results (dependent variable) and the other gridded SO datasets (independent) from MODIS, Landsat, and IMS. The residuals were calculated over a 2004–2016 common validation period spanning the Alaska domain. The PMW SO performance was assessed through pixel-wise correlations and MAE differences relative to the other established SO geospatial records. We first calculated the per pixel correlations and MAE differences between the PMW SO results and corresponding annual SO records from MODIS, Landsat, and IMS. The mean correlations and MAE differences are then aggregated by FW, FF, and TC categories to clarify the impact of these features on PMW SO performance.

## 2.6. SO Trend Analysis

We performed temporal linear trend analysis for each grid cell to estimate the sign and strength of PMW SO changes over the satellite record (1988–2016). A Theil–Sen (TS) approach was used to compute the trend slope as the median value between each paired point [59]. The TS is a robust trend estimation for non-parametric time-series that do not meet the assumptions for data normality and homoscedasticity, while also being resilient to outlier effects. Significant trends were identified using the Mann–Kendall Test (MKT) and were considered significant where  $p < 0.1$  [60].

## 3. Results

### 3.1. SNOTEL Site Validation

The MAE differences between the geospatial SO records and corresponding SO estimates defined from the in situ SNOTEL site measurements are presented in Figure 4, and stratified according to the corresponding FW, FF, and TC levels represented for each site location. Overall, the PMW SO results show a similar level of accuracy as the other benchmark SO datasets relative to the Alaska SNOTEL site observations. The mean MAE for the PMW SO results was 11.4 days across the 31 SNOTEL stations, which was intermediate between IMS and Landsat-derived SO (respective mean MAE of 9.2

and 10.8 days), and the MODIS SO record (mean MAE of 12.8 days). The PMW SO results were also within the estimated 14–16 day precision level of the SO benchmark observations, indicating favorable accuracy and performance. The PMW SO MAE values showed the strongest correspondence with the Landsat results ( $R^2 = 0.74$ ), followed by MODIS ( $R^2 = 0.72$ ) and then IMS ( $R^2 = 0.57$ ). The favorable SO performance occurred despite the much coarser spatial resolution of the PMW retrievals relative to the SO benchmark records, which was attributed to strong PMW sensitivity to snow cover conditions and the near-daily temporal fidelity of the microwave retrievals. The generally consistent SO performance also indicates a common level of uncertainty among the SO records despite the different underlying sensors and methods used for the retrievals. Thus, the performance may reflect similar spatial disparity between the landscape level SO records and local SNOTEL site measurements.

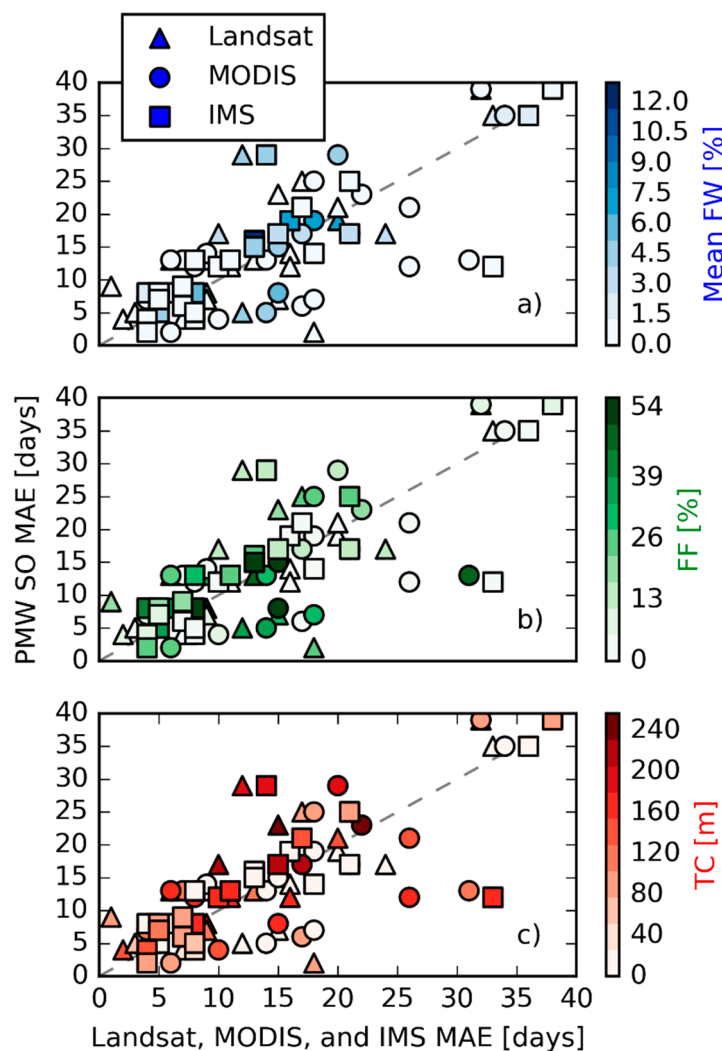


**Figure 4.** The mean absolute error (MAE) of the passive microwave (PMW) at each SNOTEL location on the y-axis and MAE for Landsat, Moderate Resolution Imaging Spectrometer (MODIS), and Ice Mapping System (IMS), identified by the shapes, on the x-axis. From top to bottom, symbols in each plot are colored by % FW, fractional water (a), % FF, fractional forest (b), and TC terrain complexity in m (c), at each respective SNOTEL location, dashed line 1:1.

There were no obvious impacts from the selected landscape heterogeneity factors on the SO MAE performance over the sparse SNOTEL locations (Figure 4). However, we compared the surface characteristics (FW, FF, TC) at each SNOTEL site location across the different SO datasets where the MAE was above or below a 14-day precision threshold. The results indicate that the PMW SO

performance was optimal (MAE < 14 days) for locations where the mean FW level was low (0.94 %), and degraded (>14 days) where the FW level was larger (4.3 %). These results are generally consistent with the expected strong PMW sensitivity to surface water [56]. However, the MODIS SO record also showed a marked decrease in MAE performance from low (0.78 %) to high (3.47%) FW levels, while the Landsat and IMS records showed only marginal SO sensitivity to FW (Table A2). The PMW SO performance was also optimal for SNOTEL locations where terrain complexity (TC) was relatively low (mean TC = 108m), and degraded at higher TC levels (112 m). The IMS and MODIS SO records also showed similar decreases in MAE performance in more complex terrain and areas of moderate FF.

The distribution of SNOTEL stations in Alaska is concentrated in the Cook Inlet and Central Interior. Four SNOTEL stations showed MAE values exceeding 21 days across each SO dataset, namely Paragon Creek, Telaquana Lake, Upper Tsaina River, and Gobblers Knob (Figure 5). The higher levels of MAE uncertainty is consistent with greater landscape heterogeneity at these locations. Paragon Creek is located at the southern edge of the Seward Peninsula within a landscape of thermokarst lakes and a mean FW of 2%. Telaquana Lake is located at the southern end of the Alaska Range and has an FW value of 13%. The Upper Tsaina River SNOTEL station is located in the Chugach Mountains and has the largest TC value (308 m) of any other SNOTEL validation site. Lastly, Gobblers Knob is located in the south facing foothill slopes of the Brooks Range where there is likely considerable wind redistribution of snow.

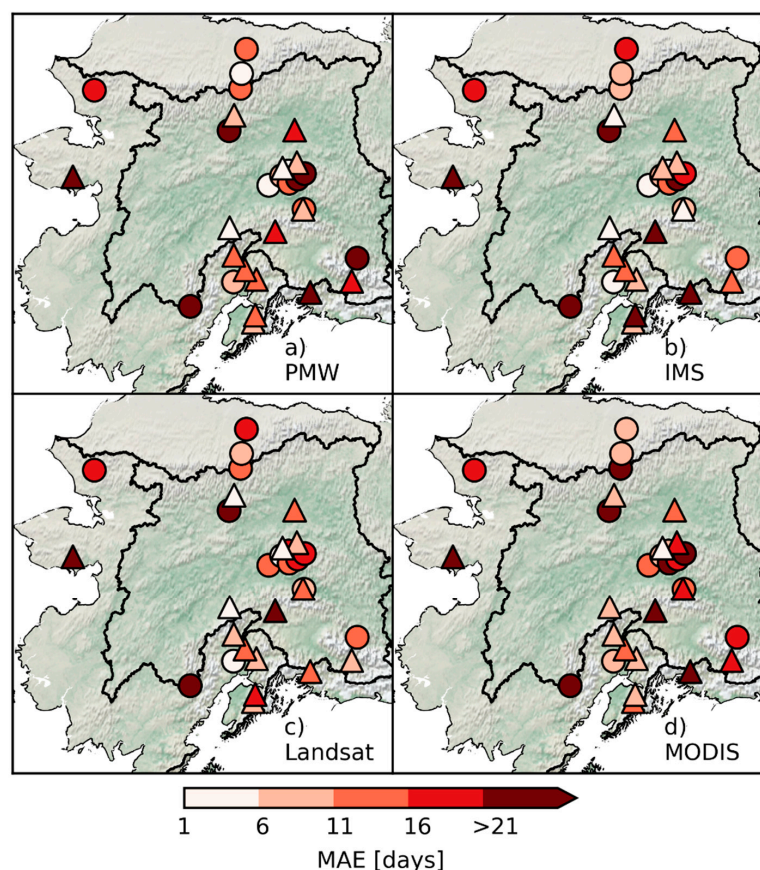


**Figure 5.** The spatial distribution of SNOTEL validation stations and their associated MAE values for PMW (a), IMS (b), Landsat (c), and MODIS (d) derived SO records. Circles indicate stations with less than ten annual SO observations for the study period and triangles indicate SNOTEL stations with SO records greater than 10 years.

The PMW SO results were compared with the other geospatial SO benchmarks and the spatially aggregated SNOTEL SO observations within three major Alaska climate zones, including North Slope,

Western, and Interior regions; the resulting annual distributions are plotted for each sub-region over the 2004 to 2016 study period (Figure 6). Overall, the PMW SO results showed similar spatial distributions and interannual variability in relation to the other geospatial SO records and available SNOTEL observations. However, the PMW and IMS results were generally more similar with each other and with the SNOTEL observations, while the Landsat and MODIS SO records showed a relatively early SO bias. The SNOTEL SO observations indicated early SO conditions in 2005 over the Alaska interior region consistent with an anomalous warm spring [61]; however, the geospatial SO records indicated more normal conditions in this region relative to the other years of record.

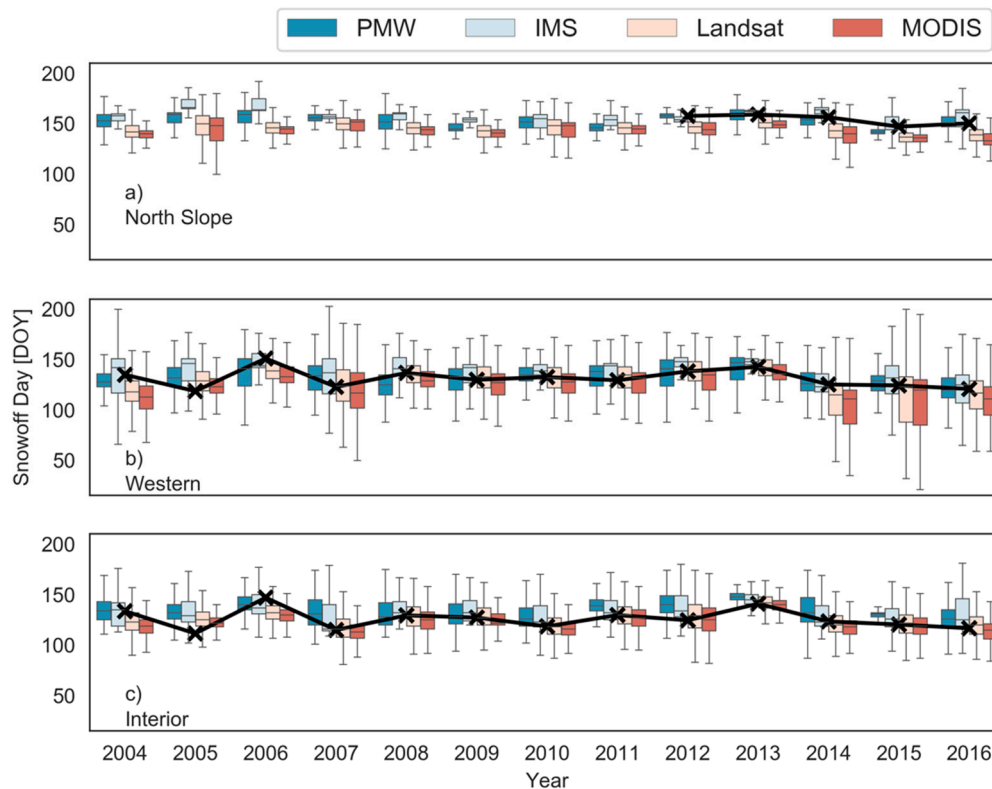


**Figure 6.** Box plot distributions of annual SO dates aggregated by Alaska climate regions over the 2004–2016 study period; “x” indicates the mean annual SO observations from in situ SNOTEL validation sites within each region. \*Note SNOTEL observations only existed from 2012–2016 in the North Slope.

Temporal correlations between the geospatial SO datasets and SNOTEL SO observations were largely significant ( $p < 0.1$ ) and similar within each climate region (Table 2). The strongest and most significant ( $p < 0.05$ ) correlations occurred in the North Slope region, despite the shorter SNOTEL record, and led by the PMW and Landsat SO results ( $R = 0.92$  and  $0.95$ , respectively). In the interior region, the PMW SO correlation ( $0.72$ ) was similar to Landsat ( $0.71$ ) and intermediate between the MODIS ( $0.76$ ) and IMS ( $0.74$ ) results. In the Western region, the PMW results showed the lowest correlation ( $0.66$ ), while the IMS record showed the best correspondence ( $0.72$ ). The MAE (RMSE) uncertainty between the geospatial SO data and SNOTEL observations ranged from 2–14 (3–14) days over the Alaska climate regions and were within the 14–16 day precision levels estimated for the IMS and Landsat SO records. In the interior region, the PMW and IMS SO records showed similar MAE (RMSE) differences of 10 (11) days that were larger than the MODIS and Landsat uncertainty of 5–6 (7–8) days. In contrast, the North Slope region showed lower PMW and IMS SO uncertainty of 2 and 4 (3 and 5) days compared with larger (14 and 11 day) uncertainty from the MODIS and Landsat records in this region.

**Table 2.** Satellite derived SO relative to SNOTEL observations, with FW and late season snow masks.

Snowoff Source	Correlation [r]			MAE [days]			RMSE [days]		
	Interior	North Slope	Western	Interior	North Slope	Western	Interior	North Slope	Western
PMW	0.72	0.92 *	0.66	10	2	5	11	3	7
IMS	0.74	0.75	0.72	10	4	7	11	5	10
Landsat	0.73	0.93 *	0.70	5	11	7	7	11	9
MODIS	0.76	0.88 *	0.71	6	14	12	8	14	14

\* Significant at  $p < 0.05$ , italics indicate no significance, otherwise all are significant at  $p < 0.01$ .

### 3.2. Residuals Distributed across Alaska

The pattern of mean residual differences (2004–2016) of the pixel-wise regression relationships between PMW SO (dependent variable) and the other (independent) SO geospatial data over Alaska are presented in Figure 7 and summarized in Table 3. The PMW results show a similar pattern of differences with the other geospatial SO records. PMW SO timing generally occurs later than the other records over colder Alaskan tundra areas of the North Slope and northern Seward Peninsula, and in higher elevation areas of the Brooks, Wrangell, Chugach, and Alaska ranges. The PMW residuals show contrasting earlier SO conditions relative to the other benchmark records over the Alaska Interior, southern, and southwest regions. Notably, the PMW SO differences are more modest relative to the IMS and are generally higher for both Landsat and MODIS in both positive and negative directions. Overall, the PMW SO results show relatively small residual differences that are within  $\pm 10$  days of the other benchmark records for a majority of the Alaska domain, including IMS (82% of study area), Landsat (70%), and MODIS (73%).

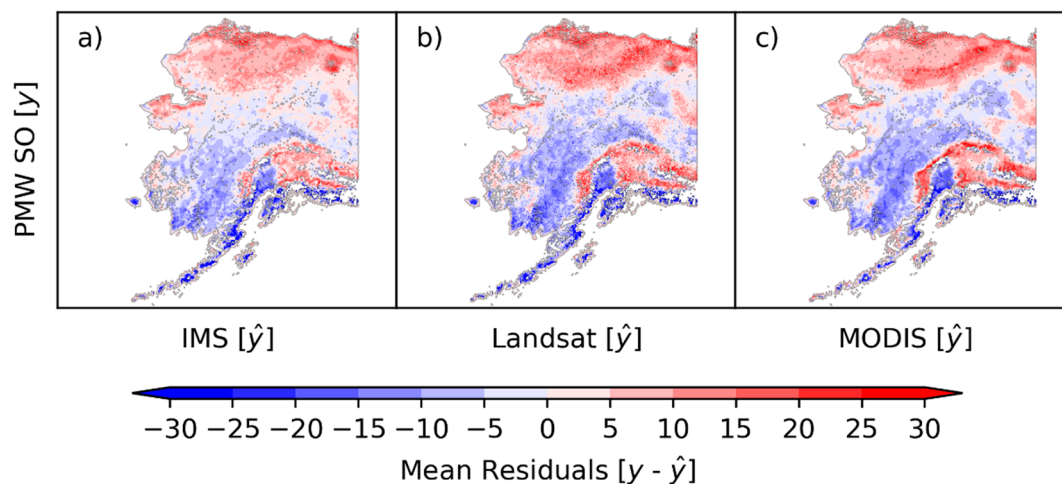


**Figure 7.** Mean residuals between PMW SO and the other SO benchmark records (IMS, Landsat, MODIS) for the 2004 to 2016 period common to all of the SO records. The blue (red) regions indicate where the PMW results show relatively early (later) SO timing relative to other geospatial SO records.

**Table 3.** Summary of mean residual differences (days) of the linear regression relationships between PMW SO timing and the other SO benchmarks over Alaska for the 2004–2016 period; the absolute area [ $\times 10^3$  km<sup>2</sup>] and relative proportion [%] of total study area represented by each residual category are shown. The regression slope coefficients are given in Table A3.

Residuals [days]	Area [ $\times 10^3$ km <sup>2</sup> ] [%]		
	IMS	Landsat	MODIS
<−20	23 [2]	26 [2]	19 [2]
−20−−10	70 [6]	124 [11]	120 [10]
−10−0	421 [36]	420 [36]	432 [37]
0−10	533 [46]	397 [34]	418 [36]
10−20	119 [10]	187 [16]	164 [14]
>20	3 [0.1]	16 [1]	16 [1]

### 3.3. Assigning Uncertainty

We calculated the pixel-wise correlations and MAE differences between the PMW SO results and each geospatial SO benchmark dataset separately to evaluate the relative performance of the PMW record over the entire Alaska domain. The mean of the subsequent correlations and MAE results were then aggregated by the different landscape factors (FW, FF, TC) to evaluate the PMW SO performance and potential degradation because of greater landscape complexity relative to the finer spatial resolution SO benchmark datasets (Figure 8). The analysis here is similar to the SNOTEL validation (Figure 4), but encompasses the entire Alaska domain rather than just the sparse SNOTEL site locations. As anticipated, we found a general decrease in PMW SO performance (MAE and correlation) with increasing FW cover. Approximately 90% of the Alaska domain showed FW levels below 6%, which contributed to favorable PMW SO average MAE (12 days) and correlation (0.53) values relative to the benchmark SO records (Figure 8a).

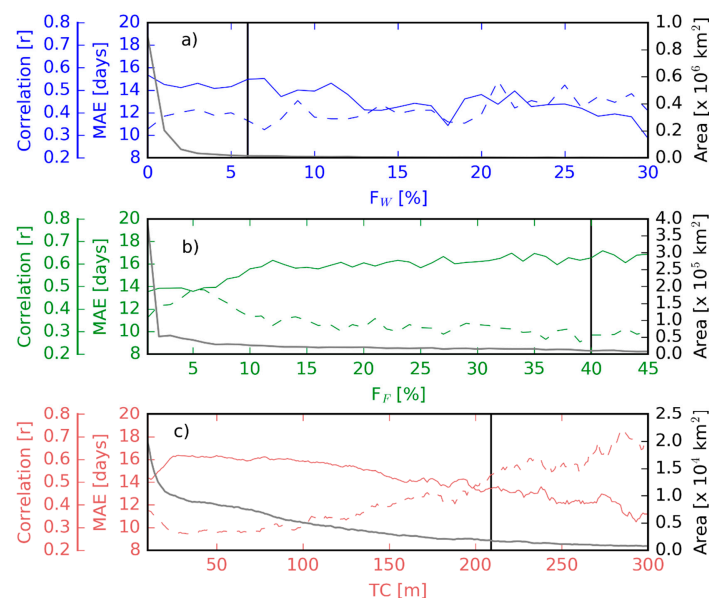


**Figure 8.** Mean absolute error (MAE) (dashed line) and correlation (solid line) between PMW SO and the other geospatial benchmark datasets over the Alaska domain, aggregated by terrain features, FW (a), FF (b), and TC (c). The grey line shows the area of the domain (Y2-axis) represented by each terrain factor (X-axis), while the black vertical lines indicate where 90% of the total area is represented. The colored dashed and solid lines denote respective MAE and correlations for each landscape factor. \*Note Area y-axes represent different scales between panels.

Surprisingly, the PMW SO results showed better MAE and correlation performance with increasing forest cover (FF). This interaction is partially attributed to generally closer agreement among the SO datasets in forested areas. Furthermore, 90% of the Alaska domain had FF coverage of less than 40% and PMW SO average MAE differences of 11 days ( $r = 0.58$ ) (Figure 8b). The PMW SO results showed degraded performance relative to the other SO benchmark datasets in areas with greater terrain complexity (TC). However, the mean MAE difference was 11 days ( $r = 0.55$ ) within 90% of the Alaska domain, which coincided with TC levels of less than 209 m. Notably, the performance was degraded where TC was between 0–20 m, which was attributed to greater PMW uncertainty contributed from water contamination of the Tb and SO retrievals in low elevation coastal areas (Figure 8c). Overall, the average MAE uncertainty of the PMW SO record was 11 days for 90% of the Alaska domain despite the diversity of landscape conditions represented from the FW, FF, and TC factors. The PMW performance over Alaska relative to the other geospatial SO datasets were similar to the accuracy level defined from the sparse SNOTEL validation sites (Section 3.1). The PMW SO performance was also within the estimated 14–16 day uncertainty threshold of the IMS and Landsat SO benchmark records.

#### 3.4. PMW SO Trends and Anomalies

We performed an analysis to determine the potential trends in annual SO timing over Alaska as defined from the long-term (1988–2016) PMW satellite record. The MKT results show both earlier and later SO trends across the Alaska domain (Figure 9). Approximately 51% and 42% of the domain showed trends toward, respective earlier and later SO timing, with 18% of these area trends significant at the 90% level. The later SO trends predominantly occur in the Russia Far East, North Slope, and Interior regions, while the earlier SO trends mainly occur near coastal margins. The relatively low level of significant trend areas is attributed to the large characteristic climate variability in Alaska relative to the more subtle environmental trends represented within the 29-year satellite record. For areas that are significant, the mean earlier trend was  $-0.39$  days  $\text{yr}^{-1}$  and ranged between  $-1.31$  and  $-0.11$  days  $\text{yr}^{-1}$ . Likewise, the mean later trend was  $0.55$  days  $\text{yr}^{-1}$  and ranged between  $0.14$  and  $0.55$  days  $\text{yr}^{-1}$ .

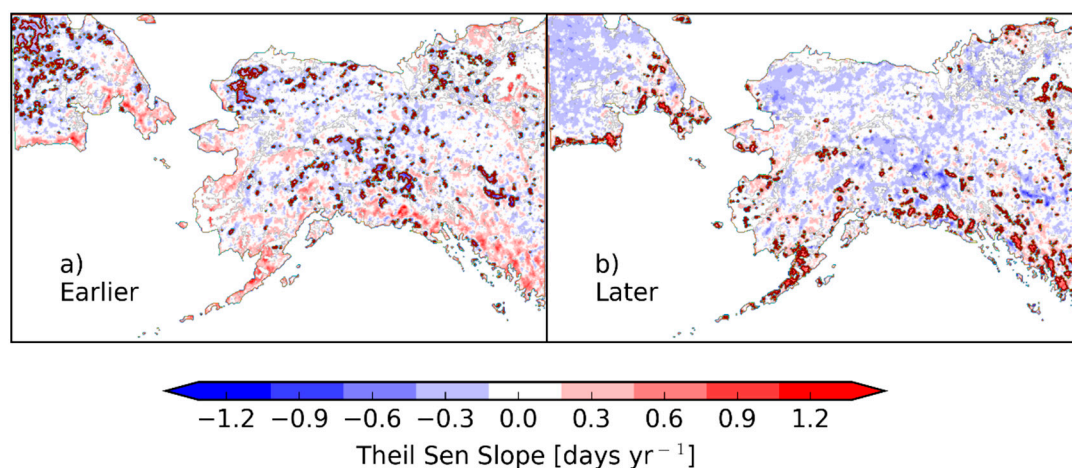


**Figure 9.** Trends in SO from 1988–2016 revealed by the PMW record. Contour lines indicate significant ( $p < 0.1$ ) earlier (a) and later (b) SO trends.

Water years 2015 and 2016 were two of the warmest years of the 29-year satellite record and are analogous to the projected future increase in mean temperatures across Alaska [62]. We evaluated the annual SO response during these anomalous warm years as a proxy for understanding future SO behavior in a warmer climate. The pixel-wise SO anomalies were derived for water years 2015 and 2016 to quantify their annual departures from average conditions defined from the 29-year PMW

record (Figure 10). The respective average surface air temperatures from January to April were 3 °C and 6 °C above-normal over the study domain for 2015 and 2016 [62].

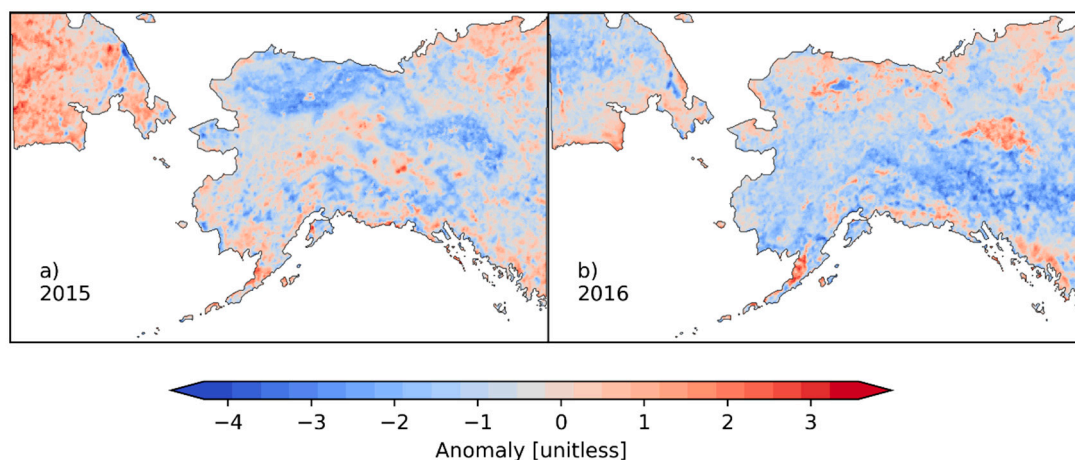


**Figure 10.** PMW SO anomalies during 2015 (a) and 2016 (b) defined from the 29-year satellite record (1988–2016).

In 2015, 47 percent ( $1.6 \times 10^6$  km<sup>2</sup>) of the domain showed anomalous early SO conditions and had an average SO day of 133, 9 days earlier than normal conditions. The anomalous early SO timing predominantly occurred over the Alaskan Arctic, but was offset by delayed SO timing over portions of the Canadian Arctic, Russian Far East, and central Alaska; where the combined area of SO delay represented 16% ( $5.6 \times 10^5$  km<sup>2</sup>) of the domain, despite generally warmer conditions.

While 2016 was also an anomalous warm year, the regional pattern of SO anomalies was quite different from the prior water year. In 2016, 65 percent ( $1.2 \times 10^6$  km<sup>2</sup>) of the domain showed anomalous early SO timing, which unlike 2015, was largely distributed across central Alaska and the Russian Far East; early SO anomaly areas in 2016 had an average SO day of 129, 13 days earlier than that overall average. Unlike the prior year, only 1% of the domain showed delayed SO timing. However, the pattern of SO delay in 2016 was largely distributed over the Alaskan Arctic and central Yukon, Canada. Collectively, these results allude to a general seasonal advance in regional SO timing under projected warming over the next few decades, but with large spatial and interannual variability driven by landscape heterogeneity in precipitation and the surface energy budget. These results also indicate the important role of both temperature and precipitation, interacting with landscape features and regional ocean-atmosphere circulation patterns, in affecting SO timing [63,64].

#### 4. Discussion

The satellite PMW SO retrieval method and results described in this study performed well in relation to independent SO estimates derived from in situ SNOTEL station measurements across Alaska ( $r = 0.66\text{--}0.92$ ; MAE = 2–10 days). The PMW SO performance at these sites was also within  $\pm 10$  days of other established geospatial SO records from the IMS, Landsat, and MODIS. These results are consistent with a prior study reporting similar PMW-derived SO accuracy over the European boreal-arctic [30]. Residual differences between the PMW SO results and more established geospatial SO records were also within  $\pm 10$  days across a majority ( $\geq 70\%$ ) of the entire Alaska domain, and below the 14–16 day estimated precision of the Landsat and MODIS derived SO products. Regional differences between the PMW SO retrievals and other SO benchmarks were attributed to the different sensitivity of optical and microwave frequencies to snow and other landscape features, as well as the different classification algorithms, spatial footprints and temporal fidelity of the observations used for the SO retrievals.

We examined the pattern of PMW SO relative errors in relation to selected landscape features expected to contribute to PMW uncertainty, including topographic complexity (TC), fractional water

(FW), and forest cover (FF) within each 6.25 km resolution PMW grid cell. Our results indicate a general decline in PMW SO performance with increasing TC, defined as the spatial standard deviation of the elevation within a grid cell. These results are consistent with the coarser footprint PMW Tb retrievals being more constrained in their ability to characterize sub-grid scale SO heterogeneity in complex landscapes relative to the finer scale optical remote sensing observations. Nevertheless, the Tb product used for this study [42,65] provides a 2–4-fold spatial resolution enhancement over other available standard PMW products for the same Tb frequencies [26,57,66], while preserving the benefit of near daily Tb temporal fidelity.

We found a smaller than expected FW influence on PMW SO uncertainty (e.g., Figure 8), despite surface water having a strong influence on microwave emissions [56]. We attributed the lower-than-expected FW sensitivity to the screening of higher FW grid cells prior to the SO algorithm implementation, and the predominantly low FW cover of the remaining 6.25 km resolution Tb grid cells used for the SO classification. However, our results indicated greater FW cover (1% increase) during anomalous warm years relative to cool years over the domain, suggesting that the enhanced water may contribute to greater PMW SO uncertainty in warmer years. High springtime FW in Alaska may be attributed to flooding of low-lying areas enhanced by snow runoff generated during a short snowmelt period when the soil is still frozen [67] and enhanced melting of permafrost [68]. Variability in annual FW is largely a response of spatial heterogeneity in climate, surface topography and permafrost conditions, but is largely governed by seasonal temperatures in the Arctic [69,70].

Surprisingly, the PMW SO results were relatively robust to increasing FF cover and even indicated improved SO consistency at higher FF levels relative to the other benchmark observations. These results contrast with prior studies indicating elevated Tb levels over Alaska interior forest regions, relative to lower Tb values expected over snow covered areas [71]. Given that the PMW SO algorithm is governed by the 19 and 37 GHz Tb difference, the expected elevation in Tb values and reduced Tb frequency gradient would be expected to reduce the effective GRP signal-to-noise ratio over dense forests [46]. Forests are also expected to attenuate microwave emissions from surface snow cover [72], further contributing to PMW SO uncertainty. The PMW record shows relatively early SO bias over much of the Alaska interior, which may reflect uncertainty contributed from the extensive forest cover in the region. The boreal forest structure tends to be closed [73], which may contribute to a stronger signal from the underlying snowpack. A stronger-than-expected microwave snow signal, coupled with significant uncertainties from optical remote sensing of snow in forested regions [21] may explain the apparent robust PMW SO response to FF.

Other factors may contribute to PMW SO uncertainty beyond the limited landscape attributes examined in this study. For example, a PMW tendency toward earlier SO timing in southwest Alaska relative to the other SO records may reflect generally shallow seasonal snow cover and tundra shrub conditions in this region, where a shallow snowpack (i.e., <5 cm depth or <10mm SWE) is largely transparent to PMW frequencies below 25 GHz [23]; while the PMW frequencies used in this study are less sensitive to shallow snow cover, the corresponding snow signal is much stronger for optical sensing in the absence of potential degradation from overlying vegetation, low solar illumination or clouds. The PMW results indicated a general 5–10 day SO delay relative to the other geospatial SO records in colder climate areas, including the Arctic North Slope, Brooks, and Alaska Ranges. This difference is within the estimated uncertainty of the SO records from Landsat and MODIS, which may be further elevated by optical remote sensing retrieval errors under unfavorable conditions including persistent cloud cover. The MODIS LCLD has been noted to precede snow depth observations [13] and is in agreement with our results showing generally early MODIS SO bias relative to the SNOTEL SO observations in the Alaska North Slope and Western regions. Both MODIS and Landsat may show similar SO uncertainty in the region because of extensive data loss from persistent cloud cover formed under orographic conditions in mountain landscapes [74], as well as shadows created from topographic complexity [75].

The PMW regional trend analysis indicated generally earlier SO conditions over approximately 51% of the domain, but with only 9% of the negative trend areas significant ( $p < 0.1$ ). These results are in general agreement with several studies showing a decline in snow cover extent and duration at higher latitudes [8,76,77], but also more diverse and of lower magnitude than expected given the Arctic amplification and increasing temperatures [3,78]. Our PMW SO trends may be tempered by the purported *global warming hiatus* which extended from 1998–2013 [79,80]. The SO trends may also be influenced by the large characteristic regional climate variability superimposed on a smaller longer-term environmental trend, and represented by a limited 29-year satellite record. However, the observed annual SO anomalies generally coincide with documented warm and cool annual temperature anomalies in the region, as temperatures have been identified as a major driver of SO timing at lower elevations [76]. As temperatures across the Arctic are projected to increase into the future [3], greater variability in snow cover conditions, including SO date, are expected.

## 5. Summary and Conclusions

The SO date is an important governor of ecologic and hydrologic processes across Alaska and Arctic-Boreal landscapes, yet a better understanding of regional patterns and trends in SO timing has been limited by a regionally sparse in situ observation network and uncertainties in geospatial SO records derived from available satellite observations and models. Uncertainties in the geospatial SO records stem from multiple factors, including different retrieval methods with variable sensitivity, spatial resolution, timing and duration of observations. In this study, we presented a satellite PMW SO retrieval method that exploits the differential response between daily 19V and 37V GHz Tb channels with daily repeat and 6.25 km resolution gridding from 1988–2016 over Alaska. The resulting PMW SO data record compliments other satellite-based SO records derived from optical remote sensing, including MODIS [13] and Landsat [31], by exploiting the unique microwave sensitivity to snow cover while extending the SO record over a longer (29-year) period. The PMW SO retrievals benefit from daily satellite Tb observations at higher latitudes ( $>50^{\circ}\text{N}$ ), but with relatively coarse spatial gridding compared with optical remote sensing-based products with finer (30 m to 500 m) spatial resolution but much coarser temporal sampling and compositing of the underlying observations because of orbital geometry, illumination, and cloud-atmosphere constraints.

The PMW SO record showed favorable accuracy in relation to independent in situ SO observations from Alaska SNOTEL weather stations ( $r = 0.66\text{--}0.92$ ; MAE = 2–10 days). The PMW accuracy at these sites was also consistent with the performance of other geospatial SO benchmarks obtained from the IMS, MODIS, and Landsat. Analysis of regression residuals between the PMW SO retrievals and other geospatial SO benchmarks indicated relative PMW SO consistency within  $\pm 10$  days of the other SO records over an average 75% of the study domain, which was also within the estimated precision of the SO benchmark observations. The PMW retrievals tended to show delayed SO timing relative to the other geospatial SO records in colder tundra and mountain areas, including the North Slope, Brooks, and Alaska Ranges; however, the PMW SO timing was comparatively early over the Alaska interior and southwest. Regional differences in SO timing were attributed to the underlying PMW and optical sensor retrievals with different sampling footprints, varying sensitivity to snow properties and potential signal degradation from cloud-atmosphere effects, surface water, vegetation cover, and terrain complexity. Despite these differences, the PMW SO performance over the entire domain was within  $\pm 11$  days of the other geospatial records, which was consistent with the in situ SNOTEL validation assessment and within the estimated precision of the SO benchmark observations.

A regional trend analysis of the 29-year PMW SO record indicated generally earlier SO timing across the domain, with a stronger tendency toward early SO conditions in anomalous warm years. Hence, as the high latitudes continue to warm, uncertainty remains in our understanding of how boreal-Arctic ecosystems and hydrological function will respond to earlier SO conditions. Our results also show snow cover persistence and SO delays in many areas, even during anomalous warm years, indicating potential resilience and refugia from climate change in the region. The global coverage and

continuing operations of PMW satellites provide the means for potential monitoring of SO conditions across the pan boreal-Arctic domain. The continuity of these observations also spans multiple decades, enhancing capabilities for distinguishing relatively subtle SO trends from a background of large characteristic regional climate variability.

**Supplementary Materials:** The PMW SO data record developed for this study is available through the NASA ORNL DAAC <https://doi.org/10.3334/ORNLDAAC/1711>.

**Author Contributions:** C.G.P., P.B.K., J.D., designed the study; C.G.P. and P.B.K. analyzed the data; all authors contributed to the writing. All authors have read and agreed to the published version of the manuscript.

**Funding:** This research was funded by the National Park Service Southwest Alaska Network, NASA Terrestrial Ecology and MEASUREs programs (NNX15AT74A, 80NSSC18K0980) in support of the Arctic Boreal Vulnerability Experiment (ABOVE).

**Acknowledgments:** We thank five anonymous reviewers for their constructive comments that improved the overall quality of this paper.

**Conflicts of Interest:** The authors declare no conflict of interest.

## Appendix A

**Table A1.** SNOTEL stations used.

Station	Elevation [m]	Latitude [dd]	Longitude [dd]
Alexander Lake	160	61.75	−150.89
Atigun Pass	4800	68.13	−149.48
Chisana	3320	62.07	−142.05
Coldfoot	1040	67.25	−150.18
Cooper Lake	1200	60.39	−149.69
Eagle Summit	3650	65.49	−145.41
Fairbanks F.O.	450	64.85	−147.8
Fort Yukon	430	66.57	−145.25
Gobblers Knob	2030	66.75	−150.67
Granite Crk	1240	63.94	−145.4
Imnaviat Creek	3050	68.62	−149.3
Independence Mine	3550	61.79	−149.28
Kantishna	1550	63.54	−150.99
Kelly Station	310	67.93	−162.28
Little Chena Ridge	2000	65.12	−146.73
May Creek	1610	61.35	−142.71
Monahan Flat	2710	63.31	−147.65
Monument Creek	1850	65.08	−145.87
Mt. Ryan	2800	65.25	−146.15
Munson Ridge	3100	64.85	−146.21
Pargon Creek	100	64.99	−163.1
Rhoads Creek	1225	63.93	−145.33
Sagwon	1000	69.42	−148.69
Summit Creek	1400	60.62	−149.53
Susitna Valley High	375	62.13	−150.04
Telaquana Lake	1275	60.98	−153.92
Teuchet Creek	1640	64.95	−145.52
Tokositna Valley	850	62.63	−150.78
Upper Chena	2850	65.1	−144.93
Upper Nome Creek	2520	65.37	−146.59
Upper Tsaina River	1750	61.19	−145.65

**Table A2.** FW, FF, and TC comparison across SO datasets where the MAE was above or below 14 days.

Source	Landcover	MAE [days]	
		<14	>14
PMW	FW [%]	0.88	5.33
PMW	FF [%]	17.38	17.83
PMW	TC [m]	113.81	64.50
IMS	FW [%]	2.06	2.25
IMS	FF [%]	20.06	6.00
IMS	TC [m]	103.56	86.00
Landsat	FW [%]	1.60	3.14
Landsat	FF [%]	19.07	14.14
Landsat	TC [m]	116.80	65.14
MODIS	FW [%]	0.64	3.55
MODIS	FF [%]	13.55	21.45
MODIS	TC [m]	104.18	96.55

**Table A3.** Regression slope coefficients used to calculate residuals.

Year	Slope Coefficients		
	PMW/IMS	PMW/Landsat	PMW/MODIS
2004	0.36	0.47	0.54
2005	0.31	0.40	0.34
2006	0.35	0.35	0.47
2007	0.48	0.44	0.38
2008	0.52	0.37	0.37
2009	0.45	0.34	0.41
2010	0.49	0.42	0.40
2011	0.29	0.24	0.27
2012	0.45	0.28	0.34
2013	0.34	0.23	0.36
2014	0.41	0.31	0.27
2015	0.26	0.25	0.23
2016	0.40	0.44	0.36
<b>Mean</b>	<b>0.39</b>	<b>0.35</b>	<b>0.37</b>

## References

- Derksen, C.; Brown, R. Spring snow cover extent reductions in the 2008–2012 period exceeding climate model projections. *Geophys. Res. Lett.* **2012**, *39*, 1–6. [[CrossRef](#)]
- Bhatt, U.S.; Walker, D.A.; Raynolds, M.K.; Comiso, J.C.; Epstein, H.E.; Jia, G.; Gens, R.; Pinzon, J.E.; Tucker, C.J.; Tweedie, C.E.; et al. Circumpolar Arctic tundra vegetation change is linked to sea ice decline. *Earth Interact.* **2010**, *14*, 1–20. [[CrossRef](#)]
- Chapin, F.S.; Sturm, M.; Serreze, M.C.; McFadden, J.P.; Key, J.R.; Lloyd, A.H.; McGuire, A.D.; Rupp, T.S.; Lynch, A.H.; Schimel, J.P.; et al. Role of land-surface changes in arctic summer warming. *Science* **2005**, *310*, 657–660. [[CrossRef](#)]
- Serreze, M.C.; Francis, J.A. The arctic amplification debate. *Clim. Chang.* **2006**, *76*, 241–264. [[CrossRef](#)]
- Stroeve, J.; Holland, M.M.; Meier, W.; Scambos, T.; Serreze, M. Arctic sea ice decline: Faster than forecast. *Geophys. Res. Lett.* **2007**, *34*, 1–5. [[CrossRef](#)]
- Du, J.; Kimball, J.S.; Duguay, C.; Kim, Y.; Watts, J.D. Satellite microwave assessment of Northern Hemisphere lake ice phenology from 2002 to 2015. *Cryosphere* **2017**, *11*, 47–63. [[CrossRef](#)]
- Liu, Z.; Kimball, J.S.; Parazoo, N.C.; Ballantyne, A.P.; Wang, W.J.; Madani, N.; Pan, C.G.; Watts, J.D.; Reichle, R.H.; Sonnentag, O.; et al. Increased high-latitude photosynthetic carbon gain offset by respiration carbon loss during an anomalous warm winter to spring transition. *Glob. Chang. Biol.* **2019**. [[CrossRef](#)] [[PubMed](#)]

8. Kim, Y.; Kimball, J.S.; Robinson, D.A.; Derksen, C. New satellite climate data records indicate strong coupling between recent frozen season changes and snow cover over high northern latitudes. *Environ. Res. Lett.* **2015**, *10*, 1–10. [[CrossRef](#)]
9. Pulliainen, J.; Aurela, M.; Laurila, T.; Aalto, T.; Takala, M.; Salminen, M.; Kulmala, M.; Barr, A.; Heimann, M.; Lindroth, A.; et al. Early snowmelt significantly enhances boreal springtime carbon uptake. *Proc. Natl. Acad. Sci. USA* **2017**, *114*, 201707889. [[CrossRef](#)]
10. Ling, F.; Zhang, T. Impact of the timing and duration of seasonal snow cover on the active layer and permafrost in the Alaskan Arctic. *Permafr. Periglac. Process.* **2003**, *14*, 141–150. [[CrossRef](#)]
11. Niittynen, P.; Heikkinen, R.K.; Luoto, M. Snow cover is a neglected driver of Arctic biodiversity loss. *Nat. Clim. Chang.* **2018**, *8*, 997–1001. [[CrossRef](#)]
12. Phoenix, G. Arctic plants threatened by winter snow loss. *Nat. Clim. Chang.* **2018**, *8*, 942–943. [[CrossRef](#)]
13. Lindsay, C.; Zhu, J.; Miller, A.E.; Kirchner, P.; Wilson, T.L. Deriving snow cover metrics for Alaska from MODIS. *Remote Sens.* **2015**, *7*, 12961–12985. [[CrossRef](#)]
14. Liston, G.E.; McFadden, J.P.; Sturm, M. Modelled changes in arctic tundra snow, energy and moisture fluxes due to increased shrubs. *Glob. Chang. Biol.* **2002**, *8*, 17–32. [[CrossRef](#)]
15. Liston, G.E.; Hiemstra, C.A. The Changing Cryosphere: Pan-Arctic Snow Trends (1979–2009). *J. Clim.* **2011**, *24*, 5691–5712. [[CrossRef](#)]
16. Bieniek, P.A.; Walsh, J.E.; Thoman, R.L.; Bhatt, U.S. Using climate divisions to analyze variations and trends in Alaska temperature and precipitation. *J. Clim.* **2014**, *27*, 2800–2818. [[CrossRef](#)]
17. Boelman, N.T.; Liston, G.E.; Gurarie, E.; Meddens, A.J.H.; Mahoney, P.J.; Kirchner, P.B.; Bohrer, G.; Brinkman, T.J.; Cosgrove, C.L.; Eitel, J.U.H.; et al. Integrating snow science and wildlife ecology in Arctic-boreal North America. *Environ. Res. Lett.* **2019**, *14*, 010401. [[CrossRef](#)]
18. Hall, D.K.; Riggs, G.A.; Foster, J.L.; Kumar, S.V. Development and evaluation of a cloud-gap-filled MODIS daily snow-cover product. *Remote Sens. Environ.* **2010**, *114*, 496–503. [[CrossRef](#)]
19. Munkhjargal, M.; Groos, S.; Pan, C.G.; Yadamsuren, G.; Yamkin, J.; Menzel, L. Multi-Source Based Spatio-Temporal Distribution of Snow in a Semi-Arid Headwater Catchment of Northern Mongolia. *Geosciences* **2019**, *9*, 53. [[CrossRef](#)]
20. Painter, T.H.; Rittger, K.; McKenzie, C.; Slaughter, P.; Davis, R.E.; Dozier, J. Retrieval of subpixel snow covered area, grain size, and albedo from MODIS. *Remote Sens. Environ.* **2009**, *113*, 868–879. [[CrossRef](#)]
21. Che, T.; Dai, L.; Zheng, X.; Li, X.; Zhao, K. Estimation of snow depth from passive microwave brightness temperature data in forest regions of northeast China. *Remote Sens. Environ.* **2016**, *183*, 334–349. [[CrossRef](#)]
22. Tedesco, M.; Miller, J. Observations and statistical analysis of combined active-passive microwave space-borne data and snow depth at large spatial scales. *Remote Sens. Environ.* **2007**, *111*, 382–397. [[CrossRef](#)]
23. Foster, J.L.; Sun, C.; Walker, J.P.; Kelly, R.; Chang, A.; Dong, J.; Powell, H. Quantifying the uncertainty in passive microwave snow water equivalent observations. *Remote Sens. Environ.* **2005**, *94*, 187–203. [[CrossRef](#)]
24. Wang, L.; Derksen, C.; Brown, R. Detection of pan-Arctic terrestrial snowmelt from QuikSCAT, 2000–2005. *Remote Sens. Environ.* **2008**, *112*, 3794–3805. [[CrossRef](#)]
25. Wang, L.; Toose, P.; Brown, R.; Derksen, C. Frequency and distribution of winter melt events from passive microwave satellite data in the pan-Arctic, 1988–2013. *Cryosphere* **2016**, *10*, 2589–2602. [[CrossRef](#)]
26. Pan, C.G.; Kirchner, P.; Kimball, J.S.; Kim, Y.; Du, J. Rain-on-snow events in Alaska, and their frequency and distribution from satellite observations. *Environ. Res. Lett.* **2018**, *13*. [[CrossRef](#)]
27. Liu, H.; Wang, L.; Jezek, K.C. Wavelet-transform based edge detection approach to derivation of snowmelt onset, end and duration from satellite passive microwave measurements. *Int. J. Remote Sens.* **2005**, *26*, 4639–4660. [[CrossRef](#)]
28. Semmens, K.A.; Ramage, J.M. Recent changes in spring snowmelt timing in the Yukon River basin detected by passive microwave satellite data. *Cryosphere* **2013**, *7*, 905–916. [[CrossRef](#)]
29. Foster, J.L. The significance of the date of snow disappearance on the arctic tundra as a possible indicator of climate change. *Arct. Alp. Res.* **1989**, *21*, 60–70. [[CrossRef](#)]
30. Metsämäki, S.; Böttcher, K.; Pulliainen, J.; Luojus, K.; Cohen, J.; Takala, M.; Mattila, O.-P.; Schwaizer, G.; Derksen, C.; Koponen, S. The accuracy of snow melt-off day derived from optical and microwave radiometer data—A study for Europe. *Remote Sens. Environ.* **2018**, *211*, 1–12. [[CrossRef](#)]
31. Macander, M.J.; Swingley, C.S.; Joly, K.; Reynolds, M.K. Landsat-based snow persistence map for northwest Alaska. *Remote Sens. Environ.* **2015**, *163*, 23–31. [[CrossRef](#)]

32. Salomonson, V.V.; Appel, I. Development of the aqua MODIS NDSI fractional snow cover algorithm and validation results. *IEEE Trans. Geosci. Remote Sens.* **2006**, *44*, 1747–1756. [[CrossRef](#)]
33. Rittger, K.; Painter, T.H.; Dozier, J. Assessment of methods for mapping snow cover from MODIS. *Adv. Water Resour.* **2013**, *51*, 367–380. [[CrossRef](#)]
34. Rees, A.; Lemmetyinen, J.; Derksen, C.; Pulliainen, J.; English, M. Remote Sensing of Environment Observed and modelled effects of ice lens formation on passive microwave brightness temperatures over snow covered tundra. *Remote Sens. Environ.* **2010**, *114*, 116–126. [[CrossRef](#)]
35. Kim, Y.; Kimball, J.S.; Glassy, J.; Du, J. An extended global Earth system data record on daily landscape freeze – thaw status determined from satellite passive microwave remote sensing. *Earth Syst. Sci. Data* **2017**, *9*, 133–147. [[CrossRef](#)]
36. Kim, Y.; Kimball, J.S.; Zhang, K.; McDonald, K.C. Satellite detection of increasing Northern Hemisphere non-frozen seasons from 1979 to 2008: Implications for regional vegetation growth. *Remote Sens. Environ.* **2012**, *121*, 472–487. [[CrossRef](#)]
37. Ramage, J.M.; Isacks, B.L. Determination of melt-onset and refreeze timing on southeast Alaskan icefields using SSM/I diurnal amplitude variations. *Ann. Glaciol.* **2002**, *34*, 391–398. [[CrossRef](#)]
38. Tedesco, M. Snowmelt detection over the Greenland ice sheet from SSM/I brightness temperature daily variations. *Geophys. Res. Lett.* **2007**, *34*, 1–6. [[CrossRef](#)]
39. Takala, M.; Pulliainen, J.; Metsamaki, S.J.; Koskinen, J.T. Detection of snowmelt using spaceborne microwave radiometer data in Eurasia from 1979 to 2007. *IEEE Trans. Geosci. Remote Sens.* **2009**, *47*, 2996–3007. [[CrossRef](#)]
40. O’Neel, S.; Hood, E.; Bidlack, A.L.; Fleming, S.W.; Arimitsu, M.L.; Arendt, A.; Burgess, E.; Sergeant, C.J.; Beaudreau, A.H.; Timm, K.; et al. Icefield-to-ocean linkages across the northern pacific coastal temperate rainforest ecosystem. *Bioscience* **2015**, *65*, 499–512. [[CrossRef](#)]
41. Bieniek, P.A.; Bhatt, U.S.; Thoman, R.L.; Angeloff, H.; Partain, J.; Papineau, J.; Fritsch, F.; Holloway, E.; Walsh, J.E.; Daly, C.; et al. Climate divisions for Alaska based on objective methods. *J. Appl. Meteorol. Climatol.* **2012**, *51*, 1276–1289. [[CrossRef](#)]
42. Brodzik, M.J.; Long, D.G.; Hardman, M.A.; Paget, A.; Armstrong, R. *MEaSUREs Calibrated Enhanced-Resolution Passive Microwave Daily EASE-Grid 2.0 Brightness Temperature ESDR, Version 1*; NASA National Snow and Ice Data Center Distributed Active Archive Center: Boulder, CO, USA, 2018.
43. Brodzik, M.; Long, D.; Hardman, M. Best Practices in Crafting the Calibrated, Enhanced-Resolution Passive-Microwave EASE-Grid 2.0 Brightness Temperature Earth System Data Record. *Remote Sens.* **2018**, *10*, 1793. [[CrossRef](#)]
44. Abdalati, W.; Steffen, K.; Otto, C.; Jezek, K.C. Comparison of brightness temperatures from SSMI instruments on the DMSP F8 and F11 satellites for Antarctica and the Greenland ice sheet. *Int. J. Remote Sens.* **1995**, *16*, 1223–1229. [[CrossRef](#)]
45. Wang, L.; Derksen, C.; Brown, R.; Markus, T. Recent changes in pan-Arctic melt onset from satellite passive microwave measurements. *Geophys. Res. Lett.* **2013**, *40*, 522–528. [[CrossRef](#)]
46. Ferraro, R.R.; Kusselson, S.; Colton, M. An introduction to passive microwave remote sensing and its applications to meteorological analysis and forecasting. *Natl. Weather Dig.* **1999**, 11–23.
47. Chang, A.T.C.; Foster, J.L.; Hall, D.K. Nimbus-7 smmr derived global snow cover parameters. *Ann. Glaciol.* **1987**, *9*, 39–44. [[CrossRef](#)]
48. Long, D.G. Scatterometer Backscatter Imaging Using Backus–Gilbert Inversion. *IEEE Trans. Geosci. Remote Sens.* **2019**, *57*, 3179–3190. [[CrossRef](#)]
49. Dolant, C.; Langlois, A.; Montpetit, B.; Brucker, L.; Roy, A.; Royer, A. Development of a rain-on-snow detection algorithm using passive microwave radiometry. *Hydrol. Process.* **2016**, *30*, 3184–3196. [[CrossRef](#)]
50. Hall, D.K.; Riggs, G.A.; Salomonson, V.V.; DiGirolamo, N.E.; Bayr, K.J. MODIS snow-cover products. *Remote Sens. Environ.* **2002**, *83*, 181–194. [[CrossRef](#)]
51. Helfrich, S.R.; Mcnamara, D.; Ramsay, B.H.; Baldwin, T.; Kasheta, T. Enhancements to, and forthcoming developments in the Interactive Multisensor Snow and Ice Mapping System (IMS). *Hydrol. Process.* **2007**, *21*, 1576–1586. [[CrossRef](#)]
52. National Ice Center. *IMS Daily Northern Hemisphere Snow and Ice Analysis at 1 km, 4 km, and 24 km Resolutions, Version 1*; National Ice Center: Boulder, CO, USA, 2008.

53. Cooper, M.J.; Martin, R.V.; Lyapustin, A.I.; McLinden, C.A. Assessing snow extent data sets over North America to inform and improve trace gas retrievals from solar backscatter. *Atmos. Meas. Tech.* **2018**, *11*, 2983–2994. [[CrossRef](#)] [[PubMed](#)]
54. Du, J.; Kimball, J.S.; Jones, L.A.; Kim, Y.; Glassy, J.; Watts, J.D. A global satellite environmental data record derived from AMSR-E and AMSR2 microwave Earth observations. *Earth Syst. Sci. Data* **2017**, *9*, 791–808. [[CrossRef](#)]
55. Kim, Y.; Kimball, J.S.; Xu, X.; Dunbar, R.S.; Colliander, A.; Derksen, C. Global assessment of the SMAP freeze/thaw data record and regional applications for detecting spring onset and frost events. *Remote Sens.* **2019**, *11*, 1317. [[CrossRef](#)]
56. Du, J.; Kimball, J.S.; Jones, L.A.; Watts, J.D. Implementation of satellite based fractional water cover indices in the pan-Arctic region using AMSR-E and MODIS. *Remote Sens. Environ.* **2016**, *184*, 469–481. [[CrossRef](#)]
57. Du, J.; Kimball, J.S.; Reichle, R.H.; Jones, L.A.; Watts, J.D.; Kim, Y. Global Satellite Retrievals of the Near-Surface Atmospheric Vapor Pressure Deficit from AMSR-E. *Remote Sens.* **2018**, *10*, 1175. [[CrossRef](#)] [[PubMed](#)]
58. Carroll, M.; Townshend, J.; Hansen, M.; DiMiceli, C.; Sohlberg, R.; Wurster, K. MODIS Vegetative Cover Conversion and Vegetation Continuous Fields BT—Land Remote Sensing and Global Environmental Change: NASA’s Earth Observing System and the Science of ASTER and MODIS. In *Remote Sensing and Digital Image Processing*; Ramachandran, B., Justice, C.O., Abrams, M.J., Eds.; Springer: New York, NY, USA, 2011; pp. 725–745. ISBN 978-1-4419-6749-7.
59. Sen, P.K. Estimates of the Regression Coefficient Based on Kendall’s Tau. *J. Am. Stat. Assoc.* **1968**, *63*, 1379–1389. [[CrossRef](#)]
60. Kendall, M.G. *Rank Correlation Methods*; Griffin: Oxford, UK, 1948.
61. NOAA National Centers for Environmental Information. *State of the Climate: National Climate Report for Spring (MAM)*; NOAA National Centers for Environmental Information: Asheville, NC, USA, 2005.
62. Walsh, J.E.; Bieniek, P.A.; Brettschneider, B.; Euskirchen, E.S.; Lader, R.; Thoman, R.L. The exceptionally warm winter of 2015/16 in Alaska. *J. Clim.* **2017**, *30*, 2069–2088. [[CrossRef](#)]
63. Stone, R.S.; Dutton, E.G.; Harris, J.M.; Longenecker, D. Earlier spring snowmelt in northern Alaska as an indicator of climate change. *J. Geophys. Res. D Atmos.* **2002**, *107*, 10–11. [[CrossRef](#)]
64. Liston, G.E.; Sturm, M. Winter precipitation patterns in arctic Alaska determined from a blowing-snow model and snow-depth observations. *J. Hydrometeorol.* **2002**, *3*, 646–659. [[CrossRef](#)]
65. Brodzik, M.J.; Billingsley, B.; Haran, T.; Raup, B.; Savoie, M.H. EASE-Grid 2.0: Incremental but Significant Improvements for Earth-Gridded Data Sets. *ISPRS Int. J. Geo-Inf.* **2012**, *1*, 32–45. [[CrossRef](#)]
66. Pan, C.G.; Kimball, J.S.; Munkhjargal, M.; Robinson, N.P.; Tjeldeman, E.; Menzel, L.; Kirchner, P.B. Role of Surface Melt and Icing Events in Livestock Mortality across Mongolia’s Semi-Arid Landscape. *Remote Sens.* **2019**, *11*, 2392. [[CrossRef](#)]
67. Woo, M.; Young, K.L. High Arctic wetlands: Their occurrence, hydrological characteristics and Sustainability. *J. Hydrol.* **2006**, *320*, 432–450. [[CrossRef](#)]
68. Bartsch, A.; Trofaier, A.M.; Hayman, G.; Sabel, D.; Schläpfer, S.; Clark, D.B.; Blyth, E. Detection of open water dynamics with ENVISAT ASAR in support of land surface modelling at high latitudes. *Biogeosciences* **2012**, *9*, 703–714. [[CrossRef](#)]
69. Watts, J.D.; Kimball, J.S.; Jones, L.A.; Schroeder, R.; McDonald, K.C. Satellite Microwave remote sensing of contrasting surface water inundation changes within the Arctic-Boreal Region. *Remote Sens. Environ.* **2012**, *127*, 223–236. [[CrossRef](#)]
70. Prowse, T.D.; Brown, K. Appearing and disappearing lakes in the Arctic and their impacts on biodiversity. *Arct. Biodivers. Trends* **2010**, *2010*, 68–70.
71. Hall, D.K.; Sturm, M.; Benson, C.S.; Chang, A.T.C.; Foster, J.L.; Garbeil, H.; Chacho, E. Passive microwave remote and in situ measurements of arctic and subarctic snow covers in Alaska. *Remote Sens. Environ.* **1991**, *38*, 161–172. [[CrossRef](#)]
72. Tedesco, M.; Jeyaratnam, J. A new operational snow retrieval algorithm applied to historical AMSR-E brightness temperatures. *Remote Sens.* **2016**, *8*, 1037. [[CrossRef](#)]
73. Jarvis, P.; Linder, S. Constraints to growth of boreal forests. *Nature* **2000**, *405*, 904–905. [[CrossRef](#)]
74. Hall, D.; Riggs, G. Accuracy assessment of the MODIS snow products. *Hydrol. Process.* **2007**, *21*, 1534–1547. [[CrossRef](#)]
75. Colby, J.D. Topographic Normalization in Rugged Terrain. *Photogramm. Eng. Remote Sens.* **1991**, *57*, 531–537.

76. Hammond, J.C.; Saavedra, F.A.; Kampf, S.K. Global snow zone maps and trends in snow persistence 2001-2016. *Int. J. Climatol.* **2018**, *38*, 4369–4383. [[CrossRef](#)]
77. Kunkel, K.E.; Robinson, D.A.; Champion, S.; Yin, X.; Estilow, T.; Frankson, R.M. Trends and Extremes in Northern Hemisphere Snow Characteristics. *Curr. Clim. Chang. Rep.* **2016**, *2*, 65–73. [[CrossRef](#)]
78. Cohen, J.; Screen, J.A.; Furtado, J.C.; Barlow, M.; Whittleston, D.; Coumou, D.; Francis, J.; Dethloff, K.; Entekhabi, D.; Overland, J.; et al. Recent Arctic amplification and extreme mid-latitude weather. *Nat. Geosci.* **2014**, *7*, 627–637. [[CrossRef](#)]
79. Watanabe, M.; Shiogama, H.; Tatebe, H.; Hayashi, M.; Ishii, M.; Kimoto, M. Contribution of natural decadal variability to global warming acceleration and hiatus. *Nat. Clim. Chang.* **2014**, *4*, 893–897. [[CrossRef](#)]
80. Trenberth, K.E.; Fasullo, J.T. An apparent hiatus in global warming? *Earth's Future* **2013**, *1*, 19–32. [[CrossRef](#)]



© 2020 by the authors. Licensee MDPI, Basel, Switzerland. This article is an open access article distributed under the terms and conditions of the Creative Commons Attribution (CC BY) license (<http://creativecommons.org/licenses/by/4.0/>).